

**Laminar Burning Speeds and Flammability Limits of CH₄/O₂
Mixtures with Varying N₂ Dilution at Sub-Atmospheric Conditions**

Alexander Bee, Michael Börner

*Institute of Space Propulsion, German Aerospace Center (DLR), Lampoldshausen,
Germany*

Alexander Bee, M.Sc. alexander.bee@dlr.de, <https://orcid.org/0000-0002-4456-8082>

Michael Börner (corresponding author), M.Sc. michael.boerner@dlr.de,
<https://orcid.org/0000-0002-3441-2869>

Laminar Burning Speeds and Flammability Limits of CH₄/O₂ Mixtures with Varying N₂ Dilution at Sub-Atmospheric Conditions

This paper presents experimentally determined laminar burning speeds (S_L) of premixed methane/oxygen/nitrogen mixtures at sub-atmospheric conditions obtained by using the constant-pressure spherical flame method. The goal of the conducted experiments was to investigate the effects of nitrogen dilution and pressure reduction on the laminar flame speed and flammability limits of methane/oxygen mixtures. Nitrogen content was varied between 3.1 and 79.3 volume percent. S_L at a target pressure of 0.5 bar was investigated. Actual pressure levels ranged between 0.506 and 0.568 bar. Experiments at 1 bar were conducted as a benchmark case of the setup compared to results from literature. The laminar flame speed is found to increase with decreasing nitrogen content and decreasing pressure. The obtained results show good agreement with simulated data using the several chemical reaction mechanisms within 4.8% for near stoichiometric mixtures. The upper flammability limit (UFL) is shown to be pressure-sensitive while the lower flammability limit (LFL) remains stationary for both pressure levels compared to reference data at 1 bar. Furthermore, the LFL is shown to stay at 6% vol methane content, independent of nitrogen dilution ratio.

Keywords: laminar flame velocity, burning speed, methane, flammability, CH₄/O₂

Introduction

In recent years the propellant combinations liquid oxygen/ liquid methane (LOx/LCH₄) and liquid oxygen/ liquid natural gas (LOx/LNG) have been an area of growing interest in the field of liquid rocket propulsion. The reasons for this are a number of distinct advantages over more traditional rocket engine propellant combinations (e.g. LOx/LH₂ or N₂O₄/ hydrazine) like non-toxicity, better storability and handling (compared to LH₂), availability, acceptable specific impulse and similar thermodynamic

characteristics with LOX simplifying the turbomachinery design of high thrust rocket engines (Bellomi et al. 2016; Asakawa et al. 2017; Hulbert E. A. et al. 2016; Blasi, R. and Häberle, J. 2016).

LNG quality can have a significant effect on various ignition and combustion related characteristics like flammability and flame speed. In addition, sub-atmospheric conditions at ignition are relevant for reaction control system thruster and upper stage engines. For combustion modelling, the experimentally verified laminar flame speed of gas mixtures is essential and serves as a starting point for characteristics of turbulent combustion dynamics.

In liquid rocket engines (LREs) a mostly inert gas like nitrogen or helium is used to purge parts of the propellant feed system, the injector head and the combustion chamber before oxygen and fuel injection and subsequent ignition. At the time of ignition residue of said purge gases can still be found inside the combustion chamber and therefore influencing ignitability, flame spreading and ignition overpressures (Wohlhüter, M. 2020). Therefore, knowledge about the laminar flame speed of O_2/CH_4 diluted with small to moderate amounts of N_2 at conditions found in LREs prior to and during ignition is needed.

Previous experimental research has already been conducted on the topic of nitrogen diluted O_2/CH_4 flames by various research groups (Oh et al. 2012, Dyakov et al. 2001; Vega et al. 2008; Slavinskaya et al. 2013). A clear focus is set on N_2 levels simulating air or air-like mixtures in the context of the energy or automotive industries. To the authors' knowledge, no existing data is available for small contaminations of N_2 , even less so for sub-atmospheric pressures. Therefore, this paper aims at identifying the flammability limits and the laminar flame speeds for sub-atmospheric pressures for premixed mixtures relevant for rocket thruster applications.

This paper is organized as follows: The following chapter describes the underlying theory of laminar flame speed development and the experimental approach for its determination as well as the data processing methods. Subsequently, the experimental results of the flammability study and the obtained flame speeds are shown and discussed. This paper ends with a conclusion from the test results.

Methodology and Experimental Setup

Theory

The experiments in this work are based on the constant pressure method using spherical flames (Faghih, M. and Chen, Z. 2016). In this method the laminar flame speed is usually determined from measuring the flame front propagation in high speed Schlieren images. By differentiating the obtained flame radius R_f over time, the stretched propagation speed with respect to the burnt gas reads as

$$S_b = \frac{dR_f}{dt} \quad (1)$$

To account for the inevitable rise in pressure inside the combustion vessel and the resulting compression-induced flow of the gas during the process a compression correction term can be additionally considered (Chen, Z. 2009). This correction starts to become relevant when the flame radius surpasses around half the combustion chamber radius for a spherical combustion vessel and can be applied by

$$S_b = \frac{dR_f}{dt} + \frac{R_f}{3\gamma \cdot P} \cdot \frac{dP}{dt} \quad (2)$$

with P being the pressure evolution inside the combustion vessel over time and γ the ratio of heat capacities.

Due to the curvature of the spherical flame front the propagation speed is affected by flame stretch. For the further process the unstretched velocity S_b^0 is required.

In general, two underlying extrapolation methods are used to determine S_b^0 : a linear and a nonlinear approach. The linear variant first proposed by Markstein (1951) and subsequently adopted by researchers (Giannakopoulos, G. 2015) reads as

$$S_b^0 = S_b + L_b K \quad (3)$$

with the Markstein length L_b and the stretch coefficient K as unknown parameters. The stretch coefficient K depends on the flame surface area A . For a spherical flame the stretch can be simplified as followed

$$K = \frac{1}{A} \frac{dA}{dt} = \frac{8\pi R_f \dot{R}_f}{4\pi R_f^2} = \frac{2\dot{R}_f}{R_f} = \frac{2}{R_f} S_b \quad (4)$$

To obtain S_b^0 , the datapoints are plotted in a $S_b - K$ diagram and linearly extrapolated for $K = 0$. The Markstein length can then be calculated via eq. 3. This method however, tends to generally overpredict the unstretched velocity, especially for small propagation velocities (de Persis et al. 2013). To achieve more precise results, a nonlinear extrapolation can be used. The basis of said method derived from the assumption of adiabatic flames with quasi-steady propagation characteristics (Buckmaster, J. 1977; Sivashinsky, G. I. 1977) is given by the evolution equation

$$\left(\frac{S_{b_i}}{S_b^0}\right)^2 \cdot \ln\left(\frac{S_{b_i}}{S_b^0}\right) = -\frac{2L_b K_i}{S_b^0} \quad (5)$$

which then can be fitted to the obtained N experimental datapoints i . This relation is also called the nonlinear quasi-steady model (NQ). The easiest way to determine the two unknown parameters in the NQ model is to minimize the following sum

$$\sum_{i=1}^N \left| \left(\frac{S_{b_i}}{S_b^0}\right)^2 \cdot \ln\left(\frac{S_{b_i}}{S_b^0}\right) + \frac{2L_b K_i}{S_b^0} \right| \quad (6)$$

This approach is generally considered to deliver more accurate results (de Persis et al. 2013) compared to the linear extrapolation. Latest work on different extrapolation methods and their applicability and accuracy has been conducted by Shu et al. (2021). While both previous methods were examined and provided results in good agreement to other experimental and simulated results, two modified equations were proposed, named modified linear curvature model (MLC) and modified nonlinear quasi-steady model (MNQ). These models can be fitted to the experimental data to obtain S_b^0 , L_b and the products thickness δ_p . These models are presented in eq. 7 and eq. 8, respectively.

$$\frac{dR_{f_i}}{dt} = S_b^0 \frac{R_{f_i} - 2L_b}{R_{f_i} + 2\delta_p} \quad (7)$$

$$\ln \frac{S_b^0}{\left(1 + \frac{2\delta_p}{R_{f_i}}\right) \cdot \frac{dR_{f_i}}{dt}} = \frac{2L_b}{R_{f_i}} \cdot \frac{S_b^0}{\left(1 + \frac{2\delta_p}{R_{f_i}}\right) \cdot \frac{dR_{f_i}}{dt}} \quad (8)$$

Sum minimization can again be used to fit the models to the obtained experimental values. Subsequently, the wanted unstretched laminar burning speed S_L is then calculated by multiplication with the density ratio α

$$S_L = \frac{\rho_b}{\rho_u} S_b^0 = \alpha \cdot S_b^0 \quad (9)$$

with ρ_b and ρ_u being the densities of the burnt and unburnt gas respectively.

Experimental Setup and Procedure

The described experiments were realized at the M3.1 test bench at the DLR Institute of Space Propulsion in Lampoldshausen, Germany. A photograph and schematic overview of the setup can be seen in figure 1.

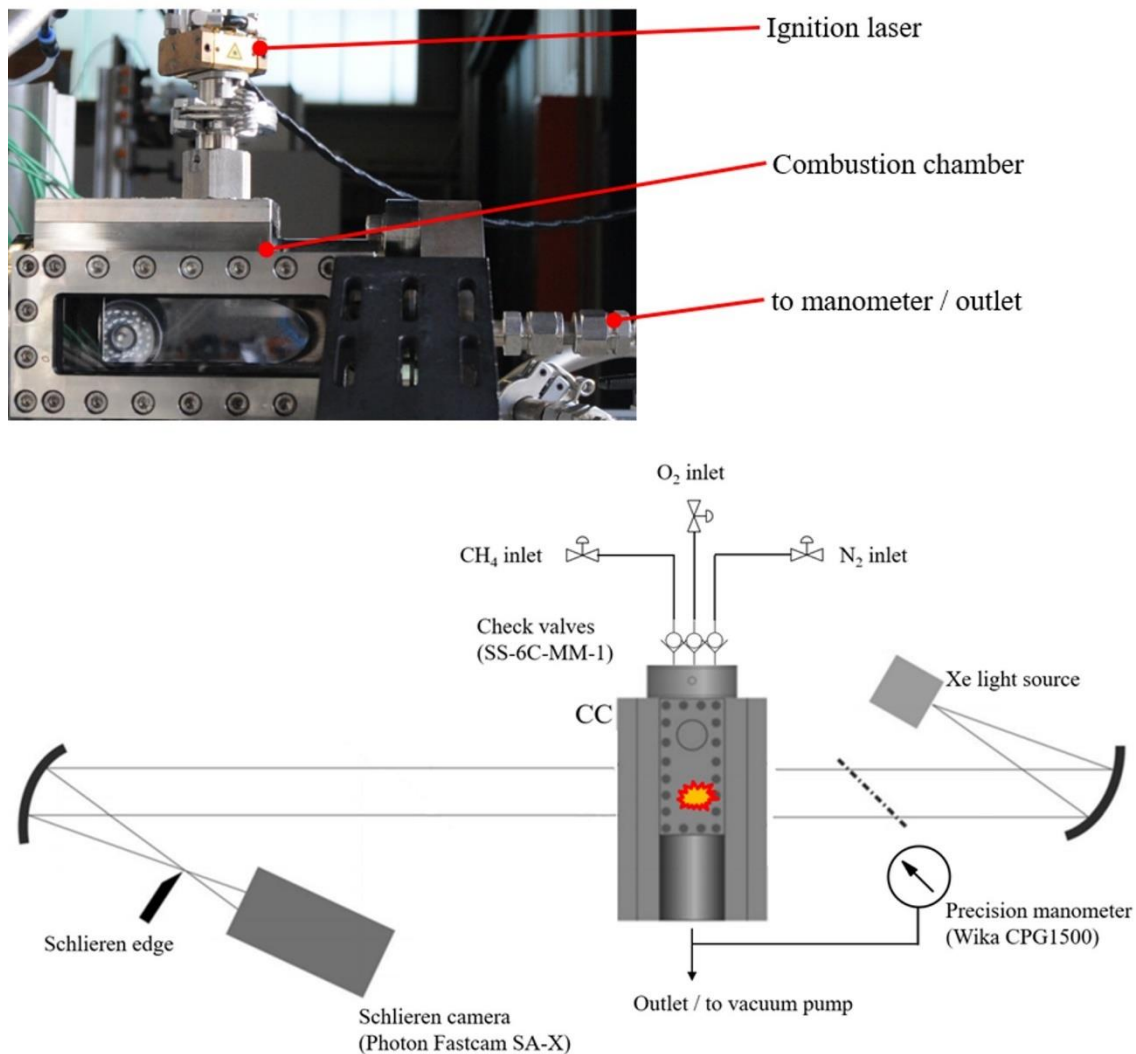


Figure 1: Photo (top left) and schematic overview (bottom) of the experimental setup at the M3.1 test bench at DLR Lampoldshausen

For this purpose, a cylindrical volume measuring 60 mm in diameter was used. The circular cross section is interrupted by two planar windows on either side of the chamber. The Schlieren imaging is performed through the two optical access windows of 35 mm height each. The used high-speed camera Photron Fastcam SA-X was set to 20000 fps with a shutter time of 1/200000 s and a resolution of 1024x512 pixels for all conducted experiments. The gases were mixed directly in the chamber using the partial pressure technique. The respective cumulative partial and total pressures were measured via a WIKA CPG-1500 high precision absolute pressure gauge with a pressure range of

0-4 bar and a nominal resolution of 0.1% FS (4 mbar). To prevent any gas counterflow or flame backlash, the feed lines are connected over three Swagelok SS-6C-MM-1 check valves with a nominal fixed opening pressure of 70 mbar (1 psi).

The experimental procedure was kept identical over all test runs. First, the chamber was completely evacuated. The pressure gradient between the chamber and ambient environment led to occurrence of leakage flow into the chamber, raising the pressure prior to working gas inlet to around 20 mbar. This additional gas was assumed as air in subsequent calculations of mixture composition. To verify this assumption, the chamber was separated from the feed lines and evacuated. The leakage rate for the setup was found to be constant with connected and disconnected feed lines, showing that the leakage flow indeed consisted of ambient air.

The gases were then introduced into the chamber starting with nitrogen. Methane was fed in last. The gases used in the experiment were methane (purity $\geq 99.5\%$) and oxygen (purity $> 99.95\%$). After a resting time of approximately 1 min. To ensure thorough mixing and reducing residual turbulence inside the vessel, the mixture was ignited with a single laser pulse with 32 mJ pulse energy and 2.3 ns FWHM focused at the center of the chamber volume. Further information on the laser and the optics can be found in a former publication of one of the authors (Börner, M. et al. 2017). The laser, as well as the camera, were triggered simultaneously via an external signal.

In total, 98 test runs at two different total starting pressure levels (ca. 1 bar and ca. 0.5 bar) with varying equivalence ratio and nitrogen content were conducted. The nitrogen content X_{N_2} was documented as the nitrogen-to-oxidizer ratio with the oxidizer

consisting of oxygen and nitrogen according to

$$X_{N_2} = \frac{p_{N_2}}{p_{O_2} + p_{N_2}} \quad (10)$$

with p_i being the respective partial pressures of the components prior to combustion.

Flammability tests were realized by setting a target mixture close to the expected value of the ignition limit. After successful or unsuccessful ignition, the target mixture was incrementally modified in direction of the limit until no ignition or ignition is reached, respectively.

To accurately determine the physical resolution of the used optical setup, an image with transparent, millimeter-gridded paper was fixed to the chamber window before testing for reference and was taken as size reference.

Data Processing

Data processing of the obtained Schlieren images was performed with a MATLAB algorithm developed in-house. The flame-edge-detection algorithm tracks the propagating flame front and determines the flame radius for every frame via gradient detection.

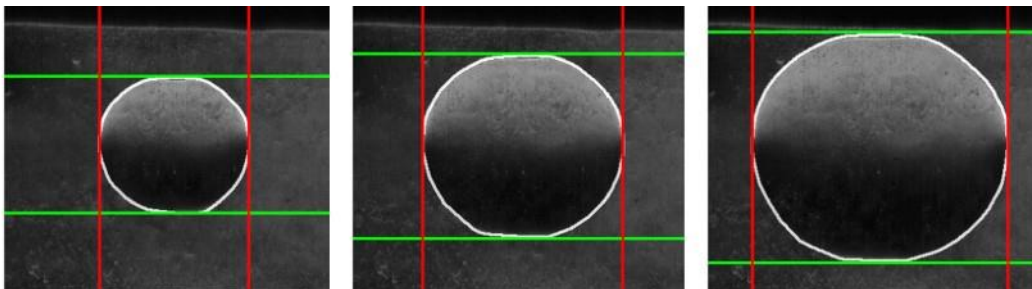


Figure 2 shows the exemplary result of the edge-tracking for a series of three frames of the same test case with 0.1 ms from frame to frame (every second frame). As shown in figure 2, the propagating flames are not perfectly spherical. This is caused by effects of

confinement resulting from the different combustion chamber dimensions in horizontal (x) and vertical (y) direction. To investigate the effects of the non-spherical propagation the flame radius was tracked in x and y direction, shown by the vertical red and horizontal green lines in figure 2 respectively. Additionally, the area A covered by the flame in every frame was detected (white outline) and used to calculate an equivalent spherical flame radius for a perfectly spherical flame with the same area

$$(R_{feq} = \sqrt{A/\pi}).$$

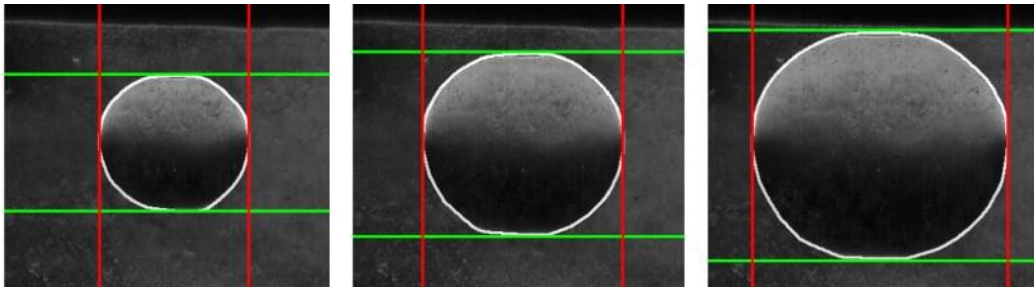


Figure 2: Schlieren image series of outwardly propagating flame front with applied automated radius detection

The determined flame radii over the time t are shown in figure 3. It is apparent, that the flame radius in x direction is larger than both the equivalent radius and the radius in y direction. Typical differences in vertical and horizontal flame radii are observed to be around 1 mm. However, only small deviations are seen for the flame propagation speed S_b . These deviations have to be considered later when estimating the experimental error margin. For further processing of the obtained data, the equivalent flame radius was

used in accordance previous research (Shu et al. 2021). The usable number of frames for data evaluation was limited by the size of the optical access window, which was only 35mm in height compared to the diameter of the combustion chamber measuring 60 mm. Additionally the first few frames in every given dataset were subject to ignition effects and had therefore also been reduced from the usable frame pool. Depending on flame propagation speed, the number of usable frames in each dataset ranged from 8 (for the high velocity test cases) to over 100 (for the low velocity test cases). With the spherical flame being positioned slightly higher than the centerline of the window, the largest usable equivalent flame radius was 14.6 mm. Therefore, the use of the pressure-rise relation presented in equation 2 in the subsequent evaluation was not necessary, as the condition $R_f > 0.5R_c$ was never fulfilled. The research provided by Burke et al.

(2009) suggests that for $R_f > 0.3R_c$ the cylindrical confinement effects are negligible.

The flames observed in this work, however, surpass this criterium which makes the inclusion of confinement error margins necessary (see chapter “Experimental Results and Discussion”).

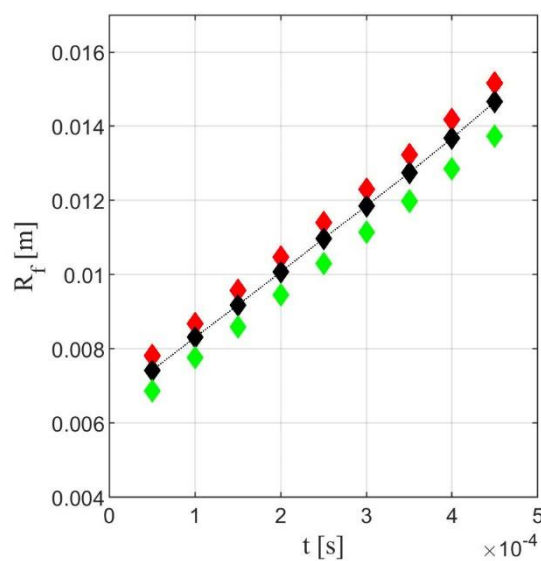


Figure 3: Detected flame radii in x (red, upper row) and y (green, lower row) direction compared to the equivalent flame radius (black, middle row)

Subsequently, the propagation speed and flame stretch are calculated for each time step. The determination of the unstretched velocity is achieved via the mentioned extrapolation models. The linear extrapolation is used to get a first estimation of S_b^0 which is then used as a starting value for the numeric minimization of the sum in equation 6. The same method delivers S_b^0 for the MLC and MNQ model. Figure shows the propagation speed extrapolation for a low and high propagation velocity test case (case #31 and #50 in table 2 respectively). For the low velocity test case (a), the overestimation of S_b^0 through the linear approach is clearly visible. The nonlinear as well as the modified models provide a lower propagation speed with sufficient agreement between each other. For higher propagation speeds (b) all methods deliver almost identical results which satisfies the expectations set by the works of de Persis et al. (2013).

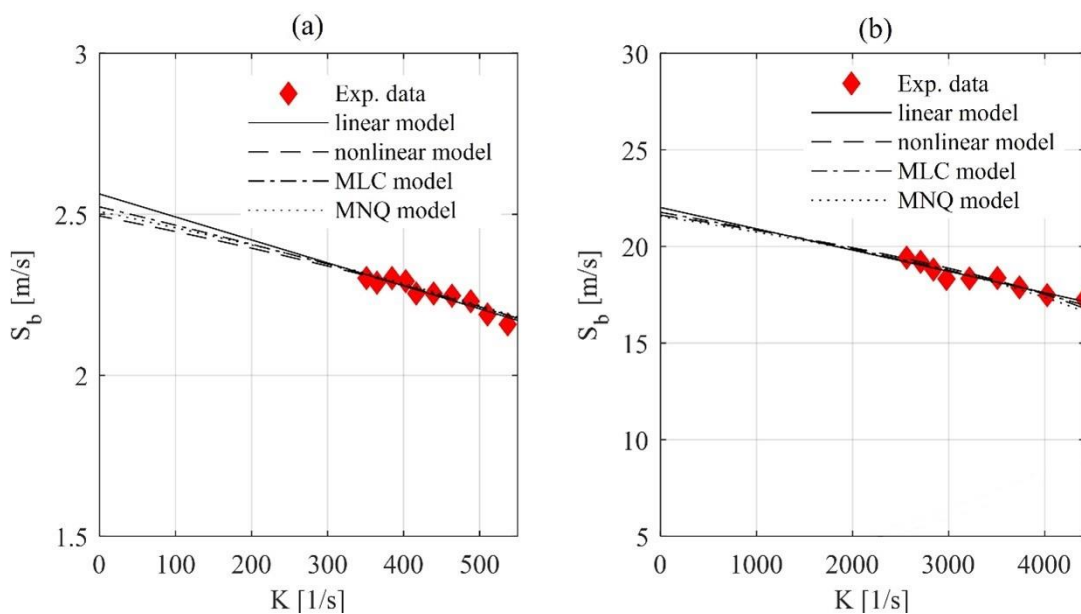


Figure 4: Example of extrapolation using the linear, NQ, MLC and MNQ models for the unstretched propagation speed of two different test cases: (a) test case #31, (b): test case #50

The density ratio of the burnt and unburnt gas is calculated with help of the NASA-CEA tool “Chemical Equilibrium with Applications” (Gordon, S. and McBride, B. J. 1996), which is used via script to determine the respective equilibrium conditions. Calculated density ratios via CEA have been benchmarked with previously used density ratios for a variety of different fuels, temperatures, pressures and mixture ratios to verify this approach: The tool delivers results within 2% of the literature for both hydrogen and heavy hydrocarbons. The same CEA tool can also be used to obtain the heat capacity ratio needed in the pressure correction term (eq. 2).

Experimental Results and Discussion

Figure 3 shows the obtained laminar flame velocities at 290 K and stoichiometric mixture ratio for the two different starting pressure levels. The values obtained experimentally are compared to simulated data using various chemical reaction mechanisms via Cantera (Goodwin et al. 2018). The used mechanisms include GRI 3.0 (Smith et al.), USC II (Wang et al. 2007) and the Aramco 3.0 mechanism (Zhou et al. 2018).

Uncertainties in mixture composition and nitrogen content due to the partial pressure mixing method are represented by horizontal error bars. The uncertainties are estimated considering the direct mixing of the gases in the evacuated combustion vessel with respect to pressure gauge accuracy, gas purity and ambient leakage flow into the chamber before injection of the gases and are therefore highly dependent on respective partial pressures for every datapoint. Therefore, error margins vary from 51% for $\Phi =$

0.144 to 3.5% for $\Phi = 2.54$. Vertical errors in the determination of S_L combine to a total of 13%. They consider variations in initial pressure and temperature (2%) and effects of confinement which were found to be in the range of 3.6% - 6.5% by Pizutti et al. (2017) for a similar setup. These confinement error margins are in rough agreement with the work of Burke et al. (2009), who report the accuracy of S_L to be within 3% for $R_F < 0.3R_{CC}$. For larger flame radii ($0.3R_{CC} < R_F < 0.5R_{CC}$) Burke et al. (2009) report uncertainties of up to 15% due to pressure and temperature rise. However, due to the relatively large aspect ratio of the used cylindrical chamber and the additional volume provided by the feed and pressure measurement lines, effects created by pressure rise are assumed to be less than those in a closed cylindrical volume used in the work of Burke et al. (2009). The effects of the non-spherical flame front caused by confinement in the used setup described earlier and shown in figure 3 are also well within these error margins. Furthermore, uncertainties in density calculation (2%), radius detection errors (increasing for low velocities near the flammability limit) at 5%, stretch calculation based on assumption of spherical, laminar flame (2%) and linear and nonlinear extrapolation uncertainty (maximum of 10% depending on frame selection) are considered. It is to be noted that for lower nitrogen content, and therefore higher flame velocities and propagation speeds, extrapolation error margins are assumed higher as a result of fewer frames available for evaluation from a single test.

In general, the data shows good agreement with the simulated values over the entire nitrogen content range. Aramco 3.0 delivers the highest values for S_L followed by

GRI 3.0. The lowest values are predicted by USC II. As expected, for lower pressure, laminar burning speed S_L is higher over the entire nitrogen dilution range compared to the 1 bar test case for both the experimental values and the simulated results.

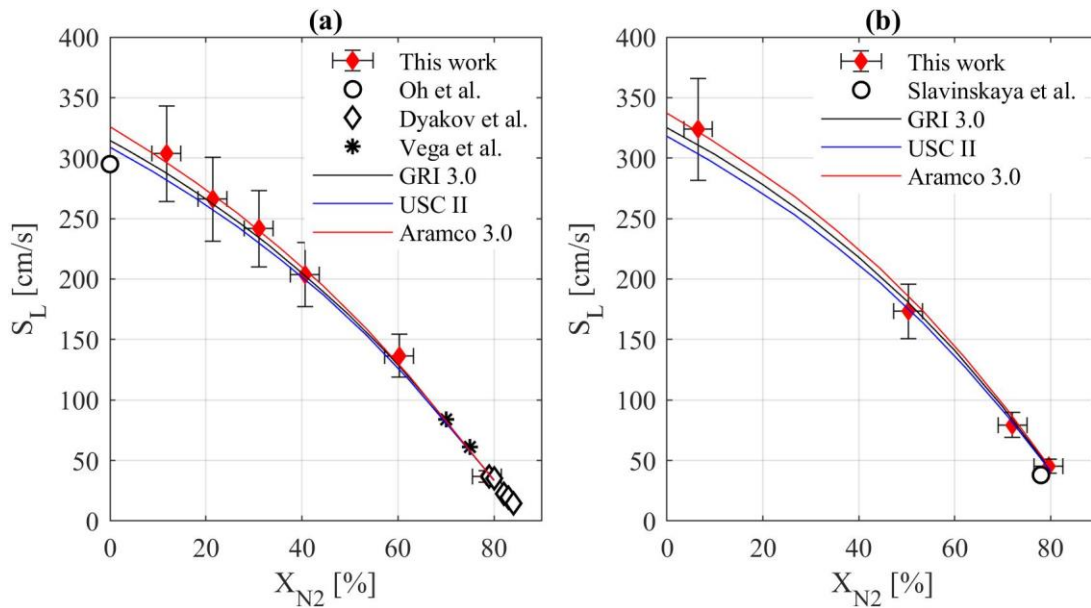


Figure 3: Experimental laminar flame speeds for (a) 1 bar and (b) 0.5 bar compared to common reaction mechanisms and literature values (Oh et al. 2012; Dyakov et al. 2001; Vega et al. 2008; Slavinskaya et al. 2013) for $\phi = 1$ and $T = 290$ K.

For low nitrogen content of 5% vol and an initial temperature of 290 K, the laminar flame speed over time is plotted over the respective equivalence ratio ϕ at a pressure of 0.5 bar in figure 6. ϕ ranges from lean to rich mixtures almost over the entire flammability range at the respective nitrogen dilution ratio. The experimental values are compared to the simulated values from the three reaction mechanisms. Figure 6 shows that the experiment was able to replicate numerical simulations over a wide span of ϕ .

Experimentally determined S_L is generally trending higher for $\phi < 1$ compared to the simulation, while being on the low side for $\phi > 1$. Again, S_L values in the near stoichiometric range calculated with Aramco 3.0 are higher compared to the other mechanisms while USC II and GRI 3.0 resulted in higher S_L for lean and rich mixtures, respectively. All results obtained in the flame speed measurements can be found in table 1 for 1 bar and table 2 for 0.5 bar in the appendices.

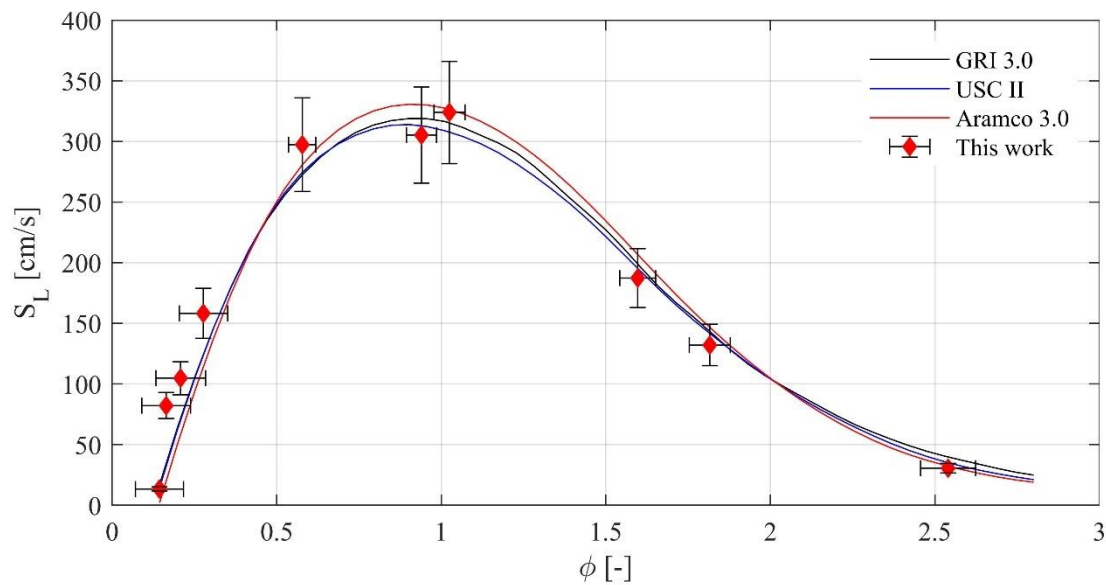


Figure 4: Experimental laminar flame velocities for low nitrogen content (5% vol) compared to GRI 3.0 for **0.5 bar** and **$T = 290$ K**.

The second part of this work is the determination of flammability limits for methane/oxygen/nitrogen mixtures at sub atmospheric pressures. While the effect of pressure reduction on the upper (UFL) and lower flammability limit (LFL) of methane/air is well researched and reported in literature (Le et al. 2012; Le et al. 2013), very little experimental data is found for mixtures with mid to low nitrogen content.

Flammability limits were determined by using the experimental setup previously used for S_L measurements. Successful and unsuccessful ignition were differentiated via the high-speed camera system and the flame propagation shortly after laser ignition. Figure 7 shows the initial flame evolution for two adjacent cases directly after ignition (every tenth frame, separated by 0.5 ms). In case (a) self-sustained propagation of the comparatively sharper flame front can be identified, while for case (b) the hot gas, produced by the laser pulse, after initial expansion remains stationary resulting in an unsuccessful ignition attempt.

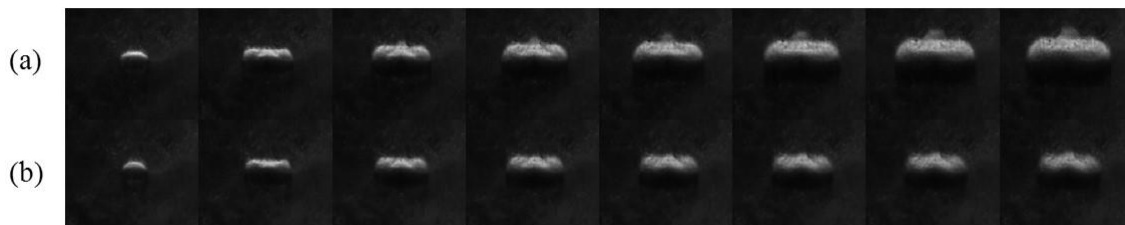


Figure 7: Schlieren image series of every tenth frame from two test cases with successful (a) (test case #97) and unsuccessful ignition (b) (test case #61) at 0.5 bar over 3.5 ms.

After the unsuccessful ignition attempt (a) the mixture was modified by adding an additional 10 mbar of oxygen, crossing the UFL to case (b). This comparison underlines the sensitivity of the test setup. The detected radius for both cases (figure 8) remains similar for both cases until approximately 0.4 ms after ignition, showing the expansion of the hot gas caused by the deposition of energy via the laser pulse. After that, the flame radius of the successful test case starts to increase signalling self-sustained combustion of the mixture.

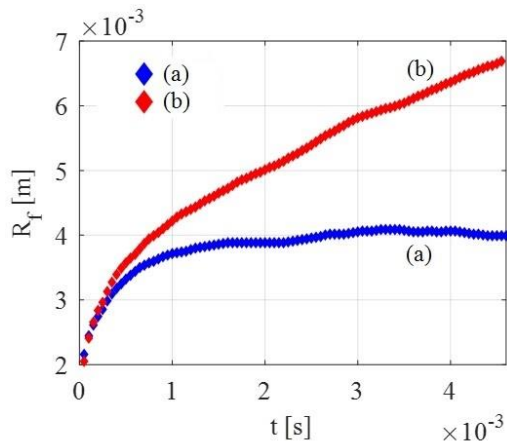


Figure 8: Flame / hot gas radius evolution over time for no ignition (a) (#97) and ignition (b) (#61)

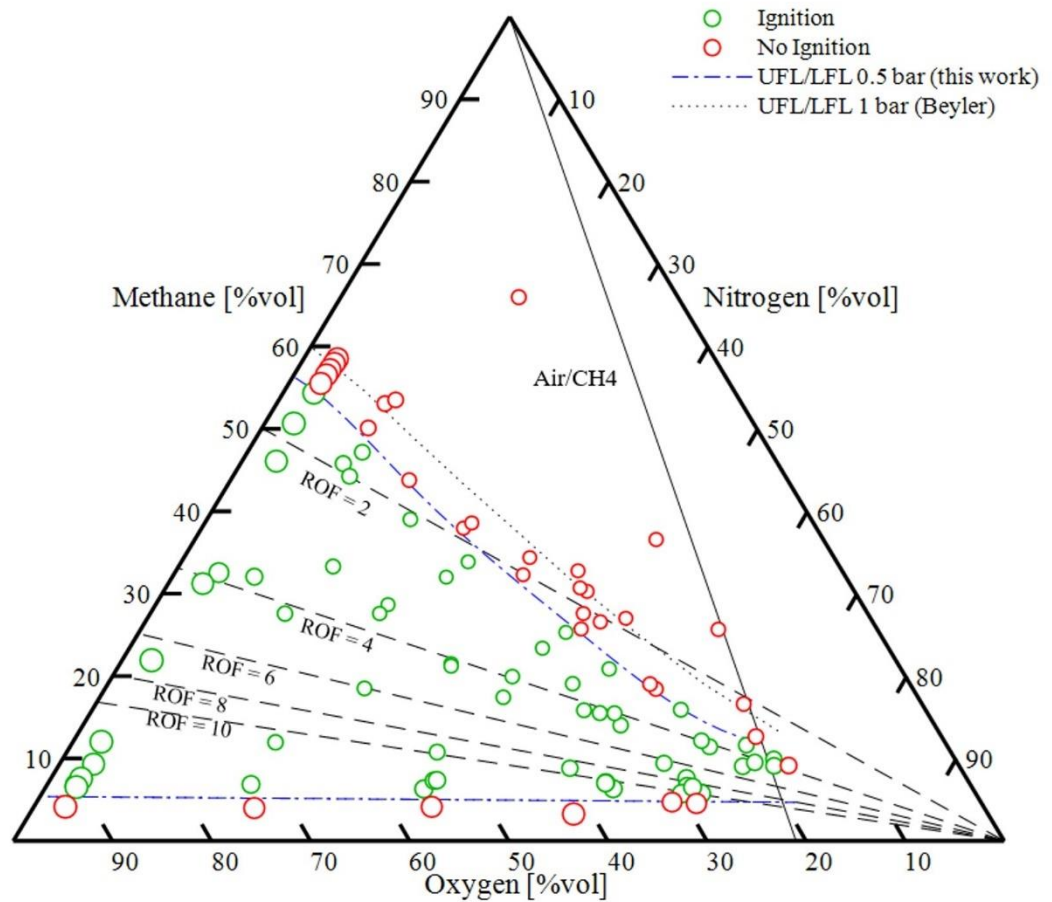


Figure 9 shows the successful and unsuccessful ignition attempts for various mixture compositions at 0.5 bar. Composition uncertainty is represented by marker radius. It is to be noted, that with a lower partial pressure of one of the three components, the error margins of mixture composition increase. This is because of the greater relative

influence of manometer resolution of 4 mbar on measurement accuracy of very low partial pressures. The broken lines represent lines of constant ROF (ratio oxidizer to fuel by mass) with a ROF of four being the stoichiometric ratio for CH_4/O_2 combustion. The “air-line”, marking the position of all possible methane/air mixtures, is also shown. As seen in

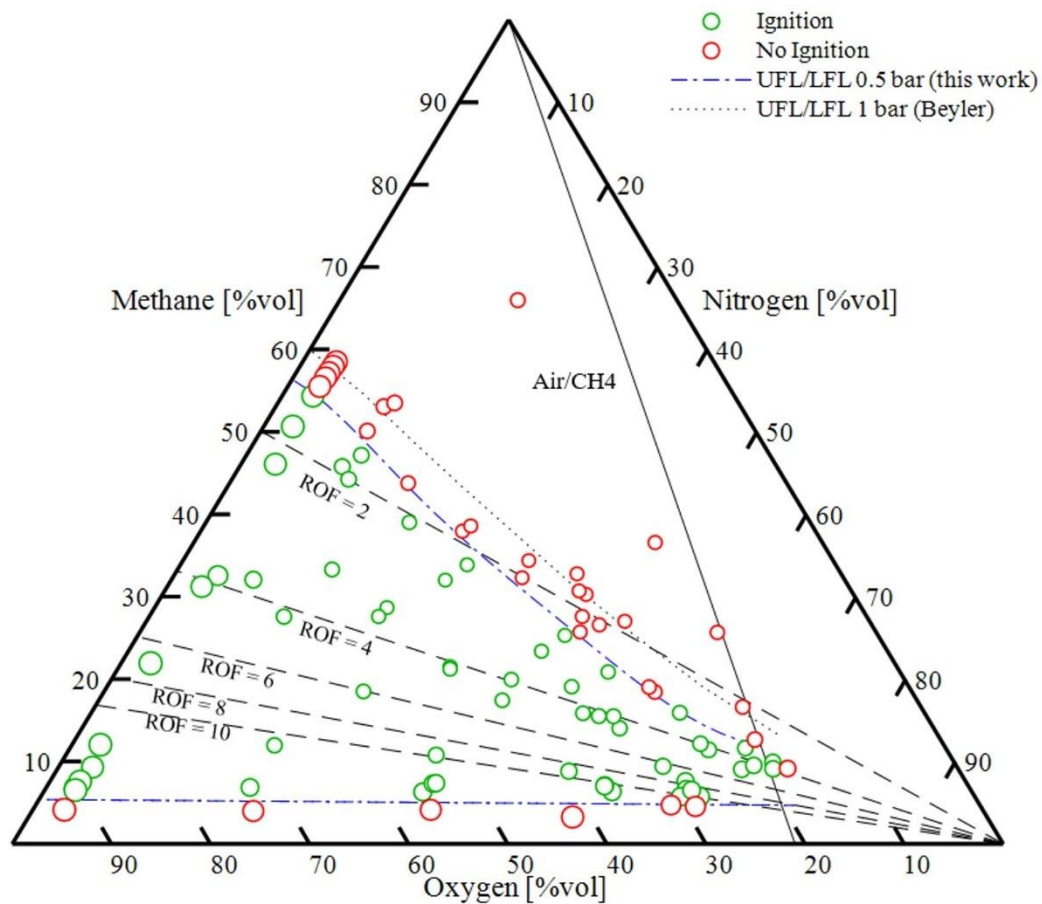


Figure 9, the LFL for 0.5 bar (blue, bottom) is unchanged over the entire nitrogen dilution realm at around 6% vol CH_4 . The UFL (blue, top) experiences a shift in ROF dependent on nitrogen content and also follow a slightly concave curve. Compared to the well-researched flammability limits at 1 bar shown as dotted line (Beyler, C. 2016), significant deviation of the UFL can be seen while the LFL remains seemingly stationary at both pressure levels. This is in agreement with the expected results based on the research by Le et al. (2013) on the UFL and by Le et al. 2012 on the LFL for

methane/air. The complete respective partial pressures of the non-flammable mixtures can be found in table 3 in the appendices. As flammability limits are generally dependent of the used ignition source, caution is advised when directly comparing these experimental results.

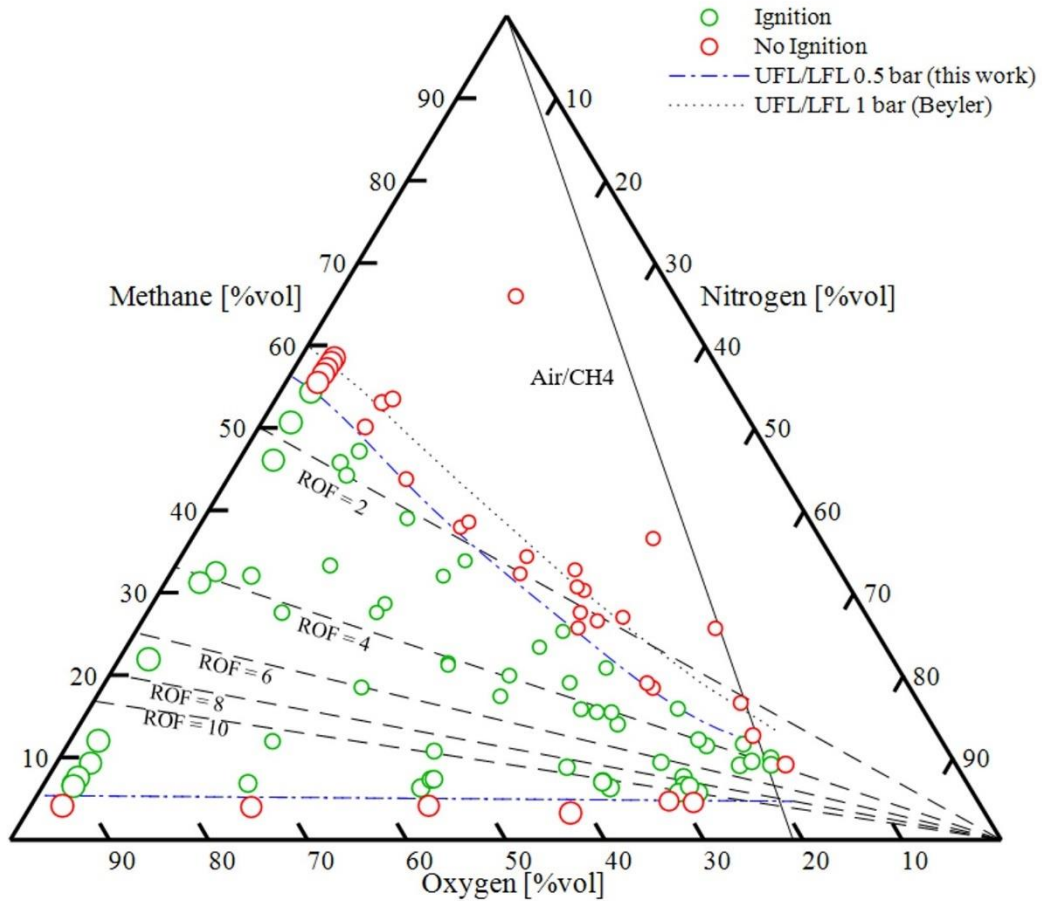


Figure 9: Flammability diagram for CH₄/O₂/N₂ mixtures at 0.5 bar, 290 K with flammability limits at 1 bar for comparison (Beyler, C. 2016). The radii of the circles represent the experimental uncertainties.

Conclusions

Laminar flame speeds for methane/oxygen/nitrogen mixtures were experimentally determined over a wide range of equivalence ratios and nitrogen content at 1 bar and 0.5 bar. Experiments were conducted in a cylindrical combustion volume, where the gaseous mixtures were ignited by a focused laser pulse. Good agreement with simulated

values using the chemical reaction mechanisms GRI 3.0, USC II and Aramco 3.0 was reached for a large nitrogen dilution span at various equivalence ratios.

Additionally, associated flammability limits for the 0.5-bar starting pressure level were experimentally determined for mixtures ranging from high nitrogen content (air) to low nitrogen content. Compared to available data at 1 bar, deviation of the UFL has been found. Reduction in pressure leads to a decrease of maximum flammable ϕ (UFL), while the LFL seemingly remains constant over the examined pressure range.

References

- Asakawa H., Nanri, H., Aoki, K., and Kubota, I. 2017. The Status of the Research and Development of LNG Rocket Engines in Japan. In De Luca, L. et al. *Chemical Rocket Propulsion*. Springer International Publishing. 463-87 doi:10.1007/978-3-319-27748-6_19.
- Bellomi, P. et al. 2019. Development of LM10-MIRA liquid oxygen – liquid natural gas expander cycle demonstrator engine. *Progress in Propulsion Physics* 11:447-66. doi:0.1051/eucass/201911447.
- Beyler, C. 2016. Flammability Limits of Premixed and Diffusion Flames. In Hurley M.J. et al. (eds) *SFPE Handbook of Fire Protection Engineering*. Springer, New York, NY. doi:10.1007/978-1-4939-2565-0_17.
- Blasi, R., and Häberle, J. 2016. LOX/methane thrust chamber demonstrator testing. Space Propulsion Conference 2016. SP2016-3124622
- Börner, M., Manfletti, C., Kroupa, G., and Oswald, M. 2017. Laser ignition of an experimental combustion chamber with a multi-injector configuration at low

- pressure conditions. *CEAS Space Journal* 9:299-311, doi:10.1007/s12567-017-0161-9.
- Buckmaster, J. 1977. Slowly varying laminar flames. *Combustion and Flame* 28:225-39. doi:10.1016/0010-2180(77)90030-X.
- Burke, M., Chen, Z., Ju, Y. and Dryer, F. 2009 Effect of cylindrical confinement on the determination of laminar flame speeds using outwardly propagating flames *Combustion and Flame* 156:771–779. doi:0.1016/J.COMBUSTFLAME.2009.01.013
- Chen, Z. 2009 Effects of compression and stretch on the determination of laminar flame speeds using propagating spherical flames. *Combustion Theory and Modelling* 13:343-64. doi:10.1080/13647830802632192
- De Persis et al. 2013. Effect of oxygen enrichment and CO₂ dilution on laminar methane flames. *Energy* 55:1055-66. doi:10.1016/j.energy.2013.04.041.
- Dyakov et al. 2001. Measurement of adiabatic burning velocity in methane-oxygen-nitrogen mixtures, *Combustion Science and Technology* 172 (1):81-96. doi:10.1080/00102200108935839.
- Faghih, M., and Chen, Z. 2016. The constant-volume propagating spherical flame method for laminar flame speed measurement. *Science Bulletin* 61:1296-310. doi:10.1007/s11434-016-1143-6.
- Giannakopoulos, G. et al. 2015. Consistent definitions of “Flame Displacement Speed” and “Markstein Length” for premixed flame propagation. *Combustion and Flame* 162 (4):49-64. doi:10.1016/j.combustflame.2014.10.01
- Goodwin, D. et al. Cantera: An object-oriented software toolkit for chemical kinetics, thermodynamics, and transport processes. <https://www.cantera.org>, 2018. Version 2.4.0. doi:10.5281/zenodo.1174508.

- Gordon, S., and McBride, B. J. 1996. Computer Program for Calculation of Complex Chemical Equilibrium Compositions and Applications. *NASA Reference Publication* 1311.
- Gu, J., and Chen, R. 2014. Modelling of Transient Stretched Laminar Flame Speed of Hydrogen- Air Mixtures Using Combustion Kinetics. *Energy Procedia* 66. doi:10.1016/j.egypro.2015.02.077.
- Hurlbert, Eric et al. 2016. International Space Exploration Coordination Group Assessment of Technology Gaps for LOx/Methane Propulsion Systems for the Global Exploration Roadmap. doi:10.2514/6.2016-5280.
- Le, H., Liu, Y., and Mannan, M. S. 2013. Lower Flammability Limits of Hydrogen and Light Hydrocarbons at Subatmospheric Pressures. *Industrial & Engineering Chemistry Research* 52:1372–378. doi:10.1021/ie302504h.
- Le, H., Nayak, S., and Mannan, M. S. 2012. Upper Flammability Limits of Hydrogen and Light Hydrocarbons in Air at Subatmospheric Pressures. *Industrial & Engineering Chemistry Research* 51:9396–402. doi:10.1021/ie300268x
- Markstein, G.H. 1951. Experimental and theoretical studies of flame-front stability. *Journal of the Aeronautical Sciences* 18:199-209.
- Oh, J., and Noh, D. 2012. Laminar burning velocity of oxy-methane flames in atmospheric condition. *Energy* 45:669-75. doi: 10.1016/j.energy.2012.07.027.
- Pizzuti, L. et al. 2017. Laminar Burning Velocity of Methane/Air Mixtures and Flame Propagation Speed Close to the Chamber Wall. *Energy Procedia* 120:126-33. doi:10.1016/j.egypro.2017.07.145.
- Shu, T., Xue, Y., Liang, W., and Ren, Z. 2021. Extrapolations of laminar flame speeds from expanding spherical flames based on the finite-structure stretched flames. *Combustion and Flame* 226:445-54. doi:10.1016/j.combustflame.2020.12.037.

- Sivashinsky, G.I. 1977. Nonlinear analysis of hydrodynamic instability in laminar flames - I. Derivation of basic equations. *Acta Astronautica* 4:1177-206.
doi:10.1016/0094-5765(77)90096-0.
- Slavinskaya, N. A. et al. 2013. Kinetic Mechanism for Low-Pressure Oxygen/Methane Ignition and Combustion. *Progress in Propulsion Physics* 4:707-32.
doi:10.2514/6.2011-94.
- Smith et al. GRI-mech3.0. <http://www.me.berkeley.edu/gri-mech/>
- Vega, E., and Kiyong, L. 2008. An experimental study on laminar CH₄/O₂/N₂ premixed flames under an electric field. *Journal of Mechanical Science and Technology* 22:312-19. doi:10.1007/s12206-007-1043-4.
- Wang, H., You, X., Joshi, A., Davis, S., Laskin, A., Egolfopoulos, F., and Law, C. 2007. USC Mech Version II. High-Temperature Combustion Reaction Model of H₂/CO/C₁-C₄ Compounds. http://ignis.usc.edu/USC_Mech_II.html
- Wollhüter, M. 2020. Experimentelle und numerische Untersuchung der Flammenentwicklung bei Laserzündung von Methan/Sauerstoff-Gemischen in Modellbrennkammern. DLR-FB-2020-41. *Institut für Raumfahrtssysteme, Universität Stuttgart*
- Zhang, X. et al. 2013. Laminar Flame Characteristics of iso-Octane/n-Butanol Blend–Air Mixtures at Elevated Temperatures. *Energy Fuels*. 27 (4):2327–35.
doi:10.1021/ef4001743
- Zhou, C-W. et al. 2018. An experimental and chemical kinetic modeling study of 1,3-butadiene combustion: Ignition delay time and laminar flame speed measurements. *Combustion and Flame* 197:423–38. doi: 10.1016/j.combustflame.2018.08.006

Appendices

Case #	p_{CH_4} [mbar]	p_{O_2} [mbar]	p_{N_2} [mbar]	X_{N_2} [%]	ϕ [-]	S_L [cm/s]
1	104	199	726	78.5	1.05	37
2	177	344	520	60.2	1.031	135
3	226	456	312	40.6	0.992	202
4	253	527	237	31	0.96	239
5	287	574	156	21.4	0.998	263
6	312	620	83	11.8	1.007	301

Table 1: Partial pressures and obtained laminar flame velocities for 1 bar starting pressure level and 290 K sorted by ascending methane content

Case #	p_{CH_4} [mbar]	p_{O_2} [mbar]	p_{N_2} [mbar]	X_{N_2} [%]	ϕ [-]	S_L [cm/s]
7	25	478	24	4.7	0.105	12
8	29	146	350	70.5	0.396	17
9	30	162	351	68.4	0.37	17
10	33	473	16	3.2	0.139	13
11	33	302	207	40.8	0.219	12
12	33	197	309	61.1	0.336	24
13	35	486	16	3.1	0.144	13
14	35	157	353	69.2	0.445	15
15	36	392	111	22	0.182	50
16	37	198	302	60.4	0.374	37
17	37	201	306	60.4	0.368	38
18	38	286	207	42.1	0.266	30
19	39	475	16	3.2	0.164	81
20	40	307	220	41.7	0.263	20
21	40	154	347	69.3	0.52	34
22	47	117	366	75.9	0.804	61
23	47	99	379	79.3	0.948	37
24	47	452	17	3.7	0.208	104
25	49	107	365	77.3	0.907	47
26	51	234	307	56.7	0.435	63
27	52	98	382	79.6	1.054	45
28	54	175	357	67.2	0.619	42
29	58	125	335	72.8	0.928	66
30	58	285	205	41.8	0.407	74
31	63	112	374	77	1.122	60
32	64	133	342	72	0.971	78
33	67	483	16	3.2	0.277	157
34	68	392	118	23.2	0.347	100
35	71	163	279	63	0.869	105
36	82	177	275	60.8	0.922	75
37	82	170	284	62.5	0.964	34
38	86	135	323	70.5	1.267	67
39	86	190	273	58.9	0.904	51
40	94	285	134	32	0.66	230
41	98	238	230	49.2	0.82	168
42	100	202	204	50.3	0.992	172
43	101	182	250	57.8	1.105	155
44	108	155	259	62.7	1.398	75
45	112	237	175	42.5	0.941	203
46	112	388	15	3.7	0.577	294

47	130	196	234	54.3	1.323	119
48	143	308	71	18.7	0.929	302
49	143	258	121	31.9	1.11	233
50	165	347	18	5	0.949	302
51	168	314	43	12.1	1.066	318
52	170	286	139	32.8	1.187	220
53	175	341	24	6.5	1.025	321
54	175	193	150	43.7	1.806	44
55	181	280	85	23.3	1.293	214
56	189	240	164	40.6	1.574	148
57	198	206	104	33.6	1.915	45
58	233	257	17	6.3	1.816	131
59	235	295	16	5.1	1.597	186
60	242	233	55	19	2.075	42
61	302	236	17	6.7	2.559	30

Table 2: Partial pressures and obtained laminar flame velocities for 0.5 bar starting pressure level and 290 K sorted by ascending methane content

Case #	p_{CH_4} [mbar]	p_{O_2} [mbar]	p_{N_2} [mbar]	X_{N_2} [%]	ϕ [-]	S_L [cm/s]
62	17	234	307	56.7	0.145	-
63	20	473	16	3.3	0.085	-
64	20	392	118	23.1	0.102	-
65	20	285	205	41.8	0.14	-
66	23	152	349	69.7	0.303	-
67	25	175	357	67.1	0.286	-
68	48	92	392	81	1.043	-
69	67	101	367	78.4	1.327	-
70	96	106	383	78.3	1.811	-
71	96	137	293	68.1	1.401	-
72	98	137	285	67.5	1.431	-
73	121	130	877	87.1	1.862	-
74	128	193	721	78.9	1.326	-
75	129	194	722	78.8	1.33	-
76	140	146	244	62.6	1.918	-
77	140	164	244	59.8	1.707	-
78	144	152	230	60.2	1.895	-
79	163	151	293	66	2.159	-
80	164	147	233	61.3	2.231	-
81	168	152	230	60.2	2.211	-
82	172	174	189	52.1	1.977	-
83	173	109	395	78.4	3.174	-
84	185	152	230	60.2	2.434	-
85	190	171	194	53.2	2.222	-
86	200	189	140	42.6	2.116	-
87	208	187	146	43.8	2.225	-
88	234	205	97	32.1	2.283	-
89	266	124	341	73.3	4.29	-
90	282	184	62	25.2	3.065	-
91	295	201	61	23.3	2.935	-
92	295	232	63	21.4	2.543	-
93	302	198	17	7.9	3.051	-
94	302	203	17	7.7	2.975	-
95	302	210	17	7.5	2.876	-
96	302	216	17	7.3	2.796	-
97	302	226	17	7	2.673	-
98	346	85	94	52.5	8.141	-

Table 3: Partial pressures of unsuccessful ignition attempts for 0.5 bar starting pressure and 290 K sorted by ascending methane content